Supporting Information

Garcia et al. 10.1073/pnas.1715451115

Anatomical Mesh Regularization with aMSM

In the original MSM algorithm (1) flexible cortical surface registration is achieved via projection of convoluted brain surfaces to a sphere. This is a common simplification inherent to other popular spherical algorithms (e.g., FreeSurfer and Spherical Demons) (2) and can be beneficial under some circumstances (e.g., removing the influence of cortical shape on cross-subject alignments of brain function). For the case of longitudinal (intrasubject) registration, however, accurate quantification of physical distortion becomes vital. For this paper, we therefore propose aMSM (available at https://github.com/ecr05/MSM_HOCR_macOSX). In this modified algorithm, correspondences between surfaces are constrained by estimated distortions between the anatomical (midthickness) surfaces. With this process, we use the locations and spacing of anatomical landmarks to obtain physically reasonable deformation gradients. Although the mathematical details of our approach have been described in ref. 3, a brief synopsis is provided below for convenience.

Strain Energy Density as an Improved, Higher-Order Regularization Penalty. Soft materials like brain tissue are often modeled as hyperelastic (the relationship between loading and deformation is nonlinear) and slightly compressible (total volume can change under loading) (4–8). These properties can be described via a strain energy density function, such as Eq. **1** of the main text, which captures the effects of 2D or 3D deformations in a scalar quantity. Because strain energy density functions represent a clear physical concept (work done by deformation-producing loads), they often separate the energies produced by isochoric deformations (change in shape) and volumetric deformations (change in size). The relationship between deformation and energy for each component can be experimentally determined and associated with shear modulus (μ) and bulk modulus (κ'), for isochoric and volumetric deformations, respectively.

In this study, we seek to minimize energetically unfavorable (thus, unlikely) deformations via a physically relevant strain energy density function, replacing the original scalar regularization penalty term in MSM. In 3D, one popular form used to describe biological soft tissues, including brain, is the classic compressible neo-Hookean model,

$$W_{3\mathrm{D}} = \frac{\mu}{2}(\bar{I}_{1,3\mathrm{D}} - 3) + \frac{\kappa'}{2}(J_{3\mathrm{D}} - 1)^2, \qquad \textbf{[S1]}$$

where $I_{1,3\mathrm{D}} = trace(\mathbf{F}_{3\mathrm{D}}^T \cdot \mathbf{F}_{3\mathrm{D}})$, $J_{3\mathrm{D}} = det(\mathbf{F}_{3\mathrm{D}})$, and $\bar{I}_{1,3\mathrm{D}} = I_{1,3\mathrm{D}}/J_{3\mathrm{D}}^{2/3}$, and $\mathbf{F}_{3\mathrm{D}}$ is the 3D deformation tensor. These terms are invariant with respect to coordinate transformation. $\bar{I}_{1,3\mathrm{D}}$ can be also written in terms of the (invariant) principal stretches as $(\lambda_1^2 + \lambda_2^2 + \lambda_3^2)/(\lambda_1\lambda_2\lambda_3)$, and $J_{3\mathrm{D}}$ can be written as $J_{3\mathrm{D}} = \lambda_1\lambda_2\lambda_3$.

Note that $\bar{I}_{1,3\mathrm{D}} - 3$ is greater than zero for shape-changing ("shear") deformations but not changes in volume. Similarly, $(J_{3\mathrm{D}} - 1)^2$ is greater than zero for size-changing ("bulk") deformations but not changes in shape. A limitation of the classic neo-Hookean form is that $(J_{3\mathrm{D}} - 1)^2$ approaches infinity as volume increases ($J_{3\mathrm{D}} \rightarrow \infty$) but just 1 as volume decreases to zero ($J_{3\mathrm{D}} \rightarrow 0$). To better match physical observations and improve numerical stability, this volumetric term is often modified to a form that also approaches infinity as volume decreases. Furthermore, for our surface analysis, modifications are necessary to approximate strain energy in 2D. To address both of these issues, we used the following modified, compressible 2D neo-Hookean form in our analysis,

$$W_{2\mathrm{D},mod} = \frac{\mu}{2}(\bar{I}_{1,2\mathrm{D}} - 2) + \frac{\kappa}{2}\left(J + \frac{1}{J} - 2\right), \qquad \textbf{[S2]}$$

where $I_{1,2\mathrm{D}} = trace(\mathbf{F}_{2\mathrm{D}}^T \cdot \mathbf{F}_{2\mathrm{D}})$, $J = det(\mathbf{F}_{2\mathrm{D}}) = \lambda_1\lambda_2$, and $\bar{I}_{1,2\mathrm{D}} = I_{1,2\mathrm{D}}/J = (\lambda_1^2 + \lambda_2^2)/(\lambda_1\lambda_2)$. In the main text, we have rewritten $\bar{I}_{1,2\mathrm{D}}$ as $\lambda_1/\lambda_2 + \lambda_2/\lambda_1 = R + 1/R$ for easier conceptualization. $R = \lambda_1/\lambda_2$ represents a new variable that conveniently describes change in 2D shape (e.g., aspect Ratio). The new form of the right-hand side was chosen to (*i*) penalize area shrinkage and expansion similarly and (*ii*) conceptually match the neo-Hookean function on the left-hand side (R and J are penalized using the same equation). The isochoric term, modulated by μ, now describes strain energy due to change in surface shape; and the volumetric term, modulated by κ, describes strain energy due to change in surface area.

In mechanical studies of actual brain tissue (3D), both gray and white matter have been found to behave as nearly incompressible materials ($\kappa' \geq 1{,}000\mu$) (5). However, our 2D analysis requires adjustment of the 3D bulk modulus into a 2D effective bulk modulus (κ) based on assumptions of either "plane stress" or "plane strain" (9). Under the assumption of plane strain, thickness of the cortex cannot deform due to in-plane forces ($\lambda_3 = 1$), and change in area relates directly to a change in volume ($\kappa \approx \kappa'$). Under the assumption of plane stress, thickness of the cortex must deform to ensure zero stress in the thickness direction; for $\kappa' \geq 1{,}000\mu$, it can be shown that the 2D effective bulk modulus is $\kappa \approx 3\mu$ (9). In reality, behavior of the cortical midthickness likely falls between these extremes: Cortical thickness is not rigidly constrained to prevent deformation, but cross-sectional models of folding also reveal developing stresses normal to the cortical surface (6). Fig. S1B' illustrates the effect of κ/μ on strain energy minimization throughout this range.

We also note that 2D strain energy minimization involves only in-plane surface distortions and displacements—it does not introduce changes in surface curvature or penalize bending. In shells, 3D strains are due to a combination of membrane strains (uniform across the shell thickness) and bending strains which vary across the thickness (higher on the outer curvature, lower on the inner curvature). Here, we have focused on membrane strain energy, considering the cortical midthickness as a rough approximation for the neutral surface (the surface at which bending strains are zero).

Using Projection to Minimize Anatomical Deformations Within a Spherical Framework. A procedure for minimizing anatomical deformations within a spherical framework was first described in ref. 4. As in that study, here we describe 3D deformation between the younger and older anatomical surfaces with $\mathbf{F}_{3\mathrm{D}} = \partial\mathbf{x}/\partial\mathbf{X}$, where $\mathbf{x}$ and $\mathbf{X}$ represent vertex coordinates on the older and younger anatomical surfaces, respectively. (Surface strain energy is calculated from $\mathbf{F}_{2\mathrm{D}}$ by considering the in-plane deformation of each anatomical face.) Similarly, projection from the younger anatomical surface to its corresponding spherical surface can be described by $\mathbf{H}_{3\mathrm{D}} = \partial\mathbf{Y}/\partial\mathbf{X}$, where $\mathbf{Y}$ represents vertex coordinates on the younger spherical surface. Projection from the older anatomical surface to its corresponding spherical surface can be described by $\mathbf{h}_{3\mathrm{D}} = \partial\mathbf{y}/\partial\mathbf{x}$, where $\mathbf{y}$ represents vertex coordinates on the older spherical surface. Deformations on the sphere—which are typically considered in spherical registration algorithms—can be defined as $\mathbf{G}_{3\mathrm{D}} = \partial\mathbf{y}/\partial\mathbf{Y}$. Note that a spherical deformation of $\mathbf{G}_{3D} = \mathbf{I}$ (the identity matrix, no deformation) will not correspond to $\mathbf{F}_{3D} = \mathbf{I}$ unless $\mathbf{x} = \mathbf{X}$ and $\mathbf{h}_{3D} = \mathbf{H}_{3D}$. Helpful schematics and further mathematical description of this process are available in ref. 4.

In Fig. 2 we defined the younger surface as the input: Its vertices will be repositioned to obtain accurate point correspondence with the older reference surface. Therefore, let us consider a second configuration, $\mathbf{Y}^*$, to represent a potential perturbation of the younger spherical surface. (Registration can also be performed in the opposite direction, which would simply reverse the terminology. We choose to denote the younger, initial surface using uppercase letters for consistency with standard notation of continuum mechanics.) Since $\mathbf{y}$, $\mathbf{Y}$, and $\mathbf{Y}^*$ represent coordinates on a sphere of a set radius, we switch from Cartesian coordinates (Y_1, Y_2, Y_3) to spherical coordinates (Θ, Φ, R), such that we need only to consider rotations in Θ and Φ directions ($r = R = R^*$). Shifted positions, $\Theta^* = \Theta + \Delta\Theta$ and $\Phi^* = \Phi + \Delta\Phi$, are projected as new anatomical locations constrained to the original anatomical surface geometry ($\mathbf{X}^*$), using barycentric interpolation. For each potential perturbation of the spherical surface ($\mathbf{Y}^*$), an average surface strain penalty is calculated from the resulting in-plane anatomical deformations ($\mathbf{X}^*$ to $\mathbf{x}$) of the surrounding faces.

aMSM Validation

To evaluate how aMSM performs under specific circumstances, we used simple geometries to test specific aspects of the registration technique. These served to validate aMSM under cases where the correct result is known and provided a starting point for optimization of more complex registration cases.

First, we validated the behavior of our strain energy minimization term (W) in the absence of data matching. For comparison with past work, we considered the same geometry as in ref. 4: a spherical surface that deforms into a "pumpkin" shape according to

$$r = 1.1(R + 0.1sin(4\Theta)cos\Phi), \quad \phi = \Phi, \quad \theta = \Theta, \qquad \textbf{[S3]}$$

shown in Fig. S1*A*. Note that, since curvature is uniform across the spherical surface, curvature matching is irrelevant in this example. However, the deformation produces strains that are not optimized (minimized) across the surface. Based on W, surface strains will be minimized differently depending on the input values for bulk (κ) and shear (μ) moduli.

Fig. S1*B*, *Top* shows the areal (J) and shape (R) components of this initial deformation. If areal and shape changes are penalized equally in aMSM ($\kappa/\mu = 1$; Fig. S1*B*, *Bottom*), both J and R are reduced and smoothed slightly. Conversely, if areal changes are penalized more heavily ($\kappa/\mu = 10$; Fig. S1*B*, *Middle*), J becomes much smoother at the expense of higher R variability. Despite algorithmic differences between aMSM and previously described finite-element approaches (4), both approaches produce similar results (Fig. S1B'). In keeping with evidence that $3 \lessapprox \kappa/\mu \lessapprox 1{,}000$ in real brain tissues (5), we choose an intermediate value of $\kappa/\mu = 10$, which produces an intermediate behavior, throughout our analysis.

Next, we consider the efficacy of curvature matching with strain energy minimization as a regularizing term (weighted by MSM input parameter Λ) to accurately align undulations on our pumpkin surface. For this, we created a second pumpkin, shifting the deformation field in Eq. **S3** by $\Delta\Theta = \pi/8$. As illustrated in Fig. S1*C*, this results in a surface with the same geometry as before but with misaligned vertices. The vertex denoted with a black star is located on an outward fold ("gyrus") on the left surface but on an inward fold ("sulcus") on the right surface.

As shown in Fig. S1*E*, *Top*, the initial configuration leads to nonzero values of strain energy density (W) and differences in curvature (Δk_{min}). For this simple case, we know that the difference between surfaces can be best described as a global affine rotation ($\Delta\Theta = \pi/8$), which results in no deformation ($W = 0$) and no differences in curvature ($\Delta k_{min} = 0$). However, since global rotation is insufficient for more complicated cases such as the folding brain, our discrete approach must be capable of producing the same alignment and deformations.

By setting regularization weight extremely high ($\Lambda \geq 10$), we approach the result of strain minimization alone (Fig. S1*E*, *Bottom*, top row). In this case, deformations and strain energy are drastically reduced, but points are not pushed toward the correct gyri and sulci (as illustrated by the remaining differences in k_{min}). Conversely, unconstrained curvature matching with very low regularization ($\Lambda \leq 0.001$) induces unrealistic deformations (Fig. S1*E*, *Bottom*, bottom row). A reasonable balance of curvature matching and strain energy minimization (optimal $\Lambda = 0.1$ for this case) achieves accurate alignment ($\Delta k_{min} = 0$, $\Delta K = 0$) and minimal distortion ($W = 0$, $J = 1$). An order of magnitude parameter sweep for the regularizing parameter, Λ, is shown in Fig. S1*D*.

aMSM Implementation Details

For the simple case described above, we saw that an optimal value of the regularizer weight parameter, Λ, could be obtained through trial and error. However, optimal balance depends on both the magnitude of deformations and the magnitude of curvature differences between surfaces, which varies for different time spans and different subjects. Furthermore, in complex brain geometries, where different areas grow and fold at different rates, the optimal balance can vary spatially within each registration. This presents a new practical issue: Too much regularization may prevent a subset of points from moving to the correct fold/position, but too little allows unrealistic deformations to develop.

For complex, variable geometries such as the brain, we modified our approach to perform two-step registration. First, we applied the lowest acceptable regularization weight ($\Lambda = 0.01$) which consistently allows each point to reach the correct gyrus or sulcus for each time span considered in this study (such that the same parameters could be used for all time spans in this study). Then we applied a heavy regularization weight ($\Lambda = 10{,}000$) to allow relaxation of unrealistic deformations, including those induced by spherical projection and overalignment of curvatures. In (a)MSM, registration of complex surfaces also progresses in a coarse-to-fine fashion, as described in Fig. S2, and Λ can be altered and optimized for each resolution level.

Since curvature matching was considered only to obtain general, initial alignment between gyri and sulci, we performed our two-step registration (balanced and then high Λ) only at low resolution levels. At higher resolution levels, after qualitative alignment had been obtained between gyri and sulci, the emphasis was shifted to strain energy minimization only (high Λ). This successfully matched each gyrus and sulcus while providing robust, smooth deformation maps at high resolution, as quantified in Table S1. Nondefault configuration parameters used in this study are shown below. With these parameters, over half of registrations completed in less than 12 h and 97% of registrations completed in less than 24 h when run on a single processor:

–CPgrid = 2,2,3,3,4,5 (Fig. S2)
–SGgrid = 4,4,5,5,6,6 (Fig. S2)
–datagrid = 4,4,5,5,6,6 (Fig. S2)
–lambda = 0.01,10000, 0.01,10000,10000,10000 (Fig. S2)
–bulkmod = 10 (Fig. S1 *A* and *B*)
–shearmod = 1 (Fig. S1 *A* and *B*)
–regoption = 3 (aMSM)
–IN (histogram matching)
–regexp = 1 (exponent on W penalty)
–kexp = 1 (exponent on R and J)
–dopt = HOCR (higher-order clique reduction)

–rescaleL (rescaled grid options at each iteration)
–it = 50,50,50,50,50,50∗

∗MSM stops running each level once it reaches convergence, usually between 10 and 20 iterations for registrations considered in this study. Here, we set an excessively high number of iterations to ensure consistent, fully converged solutions, but future optimization could consider limiting each level to fewer iterations.

Minimizing Directional Registration Bias for Accurate Growth Measurements

Finally, we address the issue that the basic MSM algorithm produces a unidirectional registration of an input surface to a reference surface. As such, differences are likely to exist between a registration of a younger surface to an older surface (forward registration) vs. registration of an older surface to a younger surface (reverse registration). To minimize any bias, we ran forward and reverse registrations for each longitudinal case. All growth maps reported in the main text represent the average of forward and reverse registrations, accomplished via a series of projections and averages in Connectome Workbench (10) (https://www.humanconnectome.org/software/get-connectome-workbench). (Each direction of registration produces a deformed version of its input sphere. To average these relationships, the inverse of the reverse registration was applied to the reference sphere. The coordinates of this sphere's vertices were then averaged with the forward registration's deformed sphere, to reduce the directional bias of registration. The inverse-reverse registration was also used to resample the growth map—always calculated from younger to older—from reverse registration into the forward framework, where it was averaged with the growth map from forward registration. The opposite of this procedure can also be used to obtain averages in the reverse framework.)

Fig. S3 quantifies observed differences between forward and reverse registrations for our largest subject group and longest time step: 30–38 wk PMA ($n = 20$). As in the main text, mean relative expansion maps are plotted for each, as well as regions of significantly higher (red) or lower (blue) expansion. As shown in Fig. S3 *A* and *B*, patterns were similar but not identical between forward and reverse aMSM registrations. Furthermore, discrepancies appear to flip for right vs. left hemisphere: e.g., relative expansion is high on the forward-registered left frontal lobe and the reverse-registered right frontal lobe. As shown in Fig. S3*C*, a paired *t* test in PALM (11) (https://fsl.fmrib.ox.ac.uk/fsl/fslwiki/PALM) revealed significant trends in the difference between forward and reverse registrations. These differences also appear to roughly flip for right vs. left hemisphere: reverse registration leads to higher relative expansion on the right lateral surface but the left medial surface. Note, however, that these differences largely cancel out when forward and reverse registrations are averaged, such that unbiased results for right and left hemispheres show nearly identical trends Fig. S3*C*.

It is important to note that right and left hemispheres were analyzed independently throughout this study. Furthermore, lateral coordinates were consistently defined such that a positive value on the right hemisphere is negative on the left hemisphere. These differences may have introduced subtle biases during surface generation (12), spherical projection, and/or optimization. As such, left and right hemispheres serve as a valuable check for consistency. Although general trends reported in this study are robust, studies which combine analysis of right and left hemispheres should carefully consider this issue and ensure proper validation.

Effect of Strain Energy Minimization on Quality of Alignment

Since the parameters for registration in this paper allow strong strain energy regularization, we performed additional tests to determine whether this could adversely affect the quality of alignment between folds; i.e., Can unconstrained minimization of strain energy (using $\kappa = 10\mu$) push initially aligned points off of the correct fold? If so, will regional differences in surface expansion dissipate under the fully converged solution? To illustrate this theoretical issue, we considered strong, regional folding of a sphere defined by $r = 1.1(R + 0.2sin(7\Theta)cos\Phi)$ if $\Theta \geq 0$, else $r = 1.1R$ (Fig. S4*A*). (In this case, the regional difference in relative surface expansion was designed to be on the order of results in Fig. 3.) By solving the problem via mechanical equations of motion, again using code modified from ref. 4, we can see the solution approaches convergence as a function of time (Fig. S4*C*). At $t = 70$ s, clear differences in relative expansion are still visible (Fig. S4*B*, *Right*). Despite large regional differences in expansion, we observe only a slight shift at the border between static and folding regions, and the distribution within each gyrus and sulcus remains reasonable (Fig. S4*D*).

While these theoretical results are useful for conceptualization, they do not prove that alignment will be maintained in discrete optimization of more complex surfaces. To examine whether alignment is maintained on an actual set of midthickness surfaces using aMSM, we revisit the representative subject in Fig. 3. Specifically, we examine the large time period (representing a more drastic change in folding) from 31 wk to 37 wk PMA (Fig. S4*E*). Fig. S4*F* plots mean curvature from the younger surface on the older surface after forward, reverse, and average aMSM registrations. In all cases, common sulci (blue) and gyri (orange) remain correctly positioned despite strong strain energy regularization at levels 2, 4, 5, and 6.

Although strong regularization via strain energy minimization worked well for these surfaces, we recognize that this solution may not be ideal for all cases. In particular, cortical midthickness reconstructions in this study had undergone careful manual editing to remove topological "holes" and other artifacts. The presence of artifactual irregularities could skew strain energy minimization and lead to unrealistic results. Furthermore, constraints on computational time may dictate the need for faster registration. These issues have been considered in ref. 3, which obtained strikingly similar results from 30 wk to term equivalent using different parameters and fewer iterations. Consistency between these results, with different surface reconstruction methods and different regularization parameters, suggests that aMSM is a robust tool for longitudinal analysis of growth.

Growth Estimates for Short and Long Time Steps

As shown in Table S4, subjects in this analysis were scanned at a variety of ages, with varying time steps between scans. To confirm that growth maps were accurate for larger time steps, we compared relative expansion maps from 30 ± 1 wk to 38 ± 2 wk PMA with and without an intermediate registration time point (34 ± 2 wk PMA). As shown in Fig. S5*A*, average expansion maps were qualitatively similar with and without the intermediate time points ($n = 8$ per group). For the case with an intermediate step, relative expansion maps (30–34 wk and 34–38 wk) were multiplied. Therefore, the higher and lower peaks observed in this case may represent multiplication of "noise" in discrete registration, rather than true growth. A paired *t* test in PALM revealed only small regions of statistically significant difference (Fig. S5*B*).

Atlas Generation

For group analysis, a 30-wk PMA group atlas was created through the following steps, as outlined in Fig. S6: In Fig. S6*A*, cortical surfaces from 18 noninjured subjects (30 ± 1 wk PMA) were affine aligned at the anterior and posterior commissures and projected to a corresponding spherical surface using CARET (13). In Fig. S6*B*, using Connectome Workbench (10), cortical surfaces were resampled to a standard 40,962-vertex mesh and averaged to create a proto-atlas. In Fig. S6*C*, individual surfaces were registered to the proto-atlas with aMSM using the same parameters described above. In Fig. S6*D*, registered surfaces were averaged in Connectome Workbench to create a final 30-wk atlas. Note that this final atlas conserves greater anatomical detail and reduces 3D dispersion (minimizes SD of the distance of subjects' vertices to the mean 3D coordinate) (Fig. S6*E*). For group analysis, all individual surfaces (time point closest to 30 wk PMA) were registered to this final 30-wk atlas.

All atlas registrations in this study used the individual's scan closest to 30 wk, so that variability between age groups did not affect our individual-to-atlas registrations. At 30 wk, variability was small between our subjects, as illustrated in Fig. S6. In future studies using multiple or different subject groups, investigators should assess variability between groups when deciding whether to use this (or another existing) atlas or whether to develop multiple group atlases for their specific research question.

1. Robinson EC, et al. (2014) MSM: A new flexible framework for multimodal surface matching. *Neuroimage* 100:414–426.
2. Yeo BT, et al. (2010) Spherical demons: Fast diffeomorphic landmark-free surface registration. *IEEE Trans Med Imaging* 29:650–668.
3. Robinson EC, et al. (2017) Multimodal surface matching with higher-order smoothness constraints. *NeuroImage* 167:453–465.
4. Knutsen AK, et al. (2010) A new method to measure cortical growth in the developing brain. *J Biomech Eng* 132:101004.
5. Chatelin S, Constantinesco A, Willinger R (2010) Fifty years of brain tissue mechanical testing: From in vitro to in vivo investigations. *Biorheology* 47:255–276.
6. Bayly P, Okamoto R, Xu G, Shi Y, Taber L (2013) A cortical folding model incorporating stress-dependent growth explains gyral wavelengths and stress patterns in the developing brain. *Phys Biol* 10:016005.
7. Tallinen T, et al. (2016) On the growth and form of cortical convolutions. *Nat Phys* 12:588–593.
8. Xu G, et al. (2010) Axons pull on the brain, but tension does not drive cortical folding. *J Biomechanical Eng* 132:071013.
9. Jasiuk I, Chen J, Thorpe M (1994) Elastic moduli of two dimensional materials with polygonal and elliptical holes. *Appl Mech Rev* 47:18–28.
10. Marcus DS, et al. (2011) Informatics and data mining tools and strategies for the human connectome project. *Front Neuroinform* 5:4.
11. Winkler AM, Ridgway GR, Webster MA, Smith SM, Nichols TE (2014) Permutation inference for the general linear model. *Neuroimage* 92:381–397.
12. Hill J, et al. (2010) A surface-based analysis of hemispheric asymmetries and folding of cerebral cortex in term-born human infants. *J Neurosci* 30:2268–2276.
13. Van Essen DC, et al. (2001) An integrated software suite for surface-based analyses of cerebral cortex. *J Am Med Inform Assoc* 8:443–459.

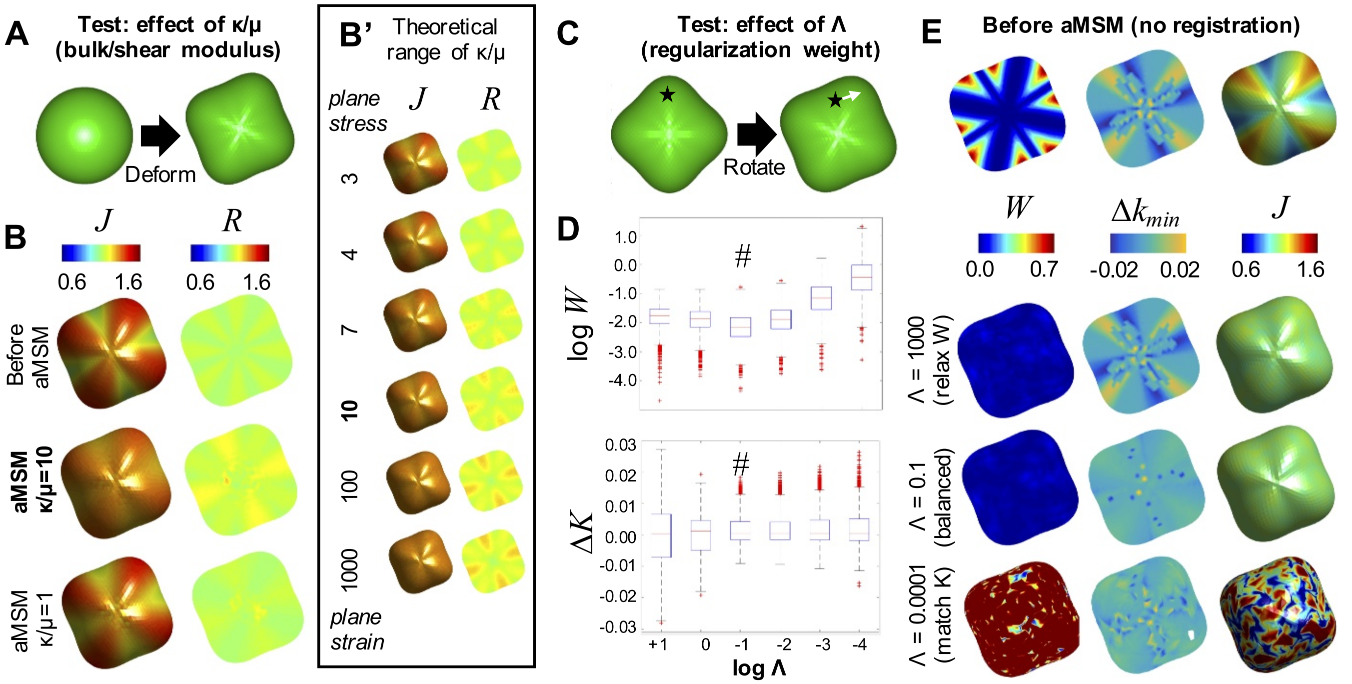

Fig. S1. aMSM parameter effects on simple undulating geometry. (*A*) Effect of bulk-shear ratio (κ/μ) was explored by minimizing surface strain energy between a sphere and pumpkin. (*B*) Areal changes (*J*) and shape changes (*R*) are not minimized in the initial, mathematically generated pumpkin shape (*Top*). Using aMSM, equal values of κ and μ smooth both *J* and *R* moderately (*Bottom*). By contrast, increasing κ reduces *J* at the expense of more variable *R* (*Top*). (*B′*) For comparison, *J* and *R* distributions for the full theoretical range of κ/μ were calculated using code modified from ref. 1. (*C*) Effect of regularization weight (Λ) was explored by aligning a shape shifted by affine rotation. (*D*) Parameter sweep reveals an optimal range of Λ that minimizes both strain energy (*W*) and mean curvature differences (ΔK). For registration at each Λ, distribution of vertex values is represented by boxplots, with outliers denoted by red + symbols and optimal solution denoted by #. (*E*) Distributions of strain energy, curvature differences, and *J* before (*Top*) and after (*Bottom*) registration. Solutions near the optimal Λ (*Bottom*, middle row) accurately moved points to approximate the true affine rotation solution ($W = 0$, $\Delta k_{min} = 0$, $J = 1$). Note that for illustration we show change in minimum curvature, k_{min}, which appeared most pronounced. Changes were similar for $K = 0.5(k_{min} + k_{max})$.

1. Knutsen AK, et al. (2010) A new method to measure cortical growth in the developing brain. *J Biomech Eng* 132:101004.

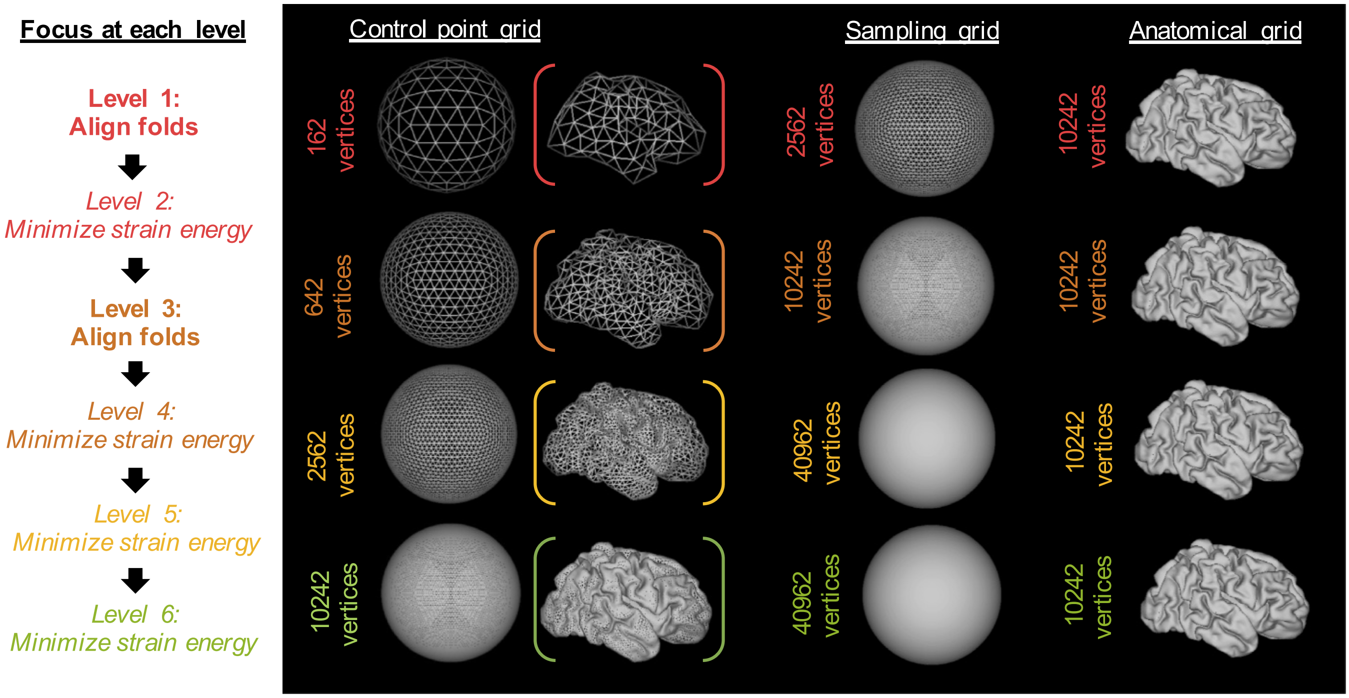

Fig. S2. aMSM optimized for complex, variable geometries. For speed and robustness, MSM aligns complex surfaces in "levels," starting with a coarse (low resolution) representation of the input and reference surfaces and then progressively moving to higher resolutions. From *Left* to *Right* in black box: (*Left*) The internal control point grid (CPgrid, points to be moved/optimized) begins as a very basic representation of the cortex. Illustration of how this grid is distributed on a cortex is shown in parentheses to *Right*. (*Center*) The corresponding sampling grid (SGgrid, set of locations to which control points can move) is typically set to a higher resolution. (*Right*) For increased accuracy, anatomical strains were calculated at a default resolution (anatgrid) of 10,242 vertices, the maximum for our final CPgrid for all levels, for each level within aMSM optimization. Low resolutions were optimized twice: first with a "balanced" $\Lambda = 0.01$, the highest value that consistently allowed each point to reach the correct gyri and sulci, and then with a high $\Lambda = 10{,}000$ to minimize unrealistic deformations after accurate alignment had been achieved.

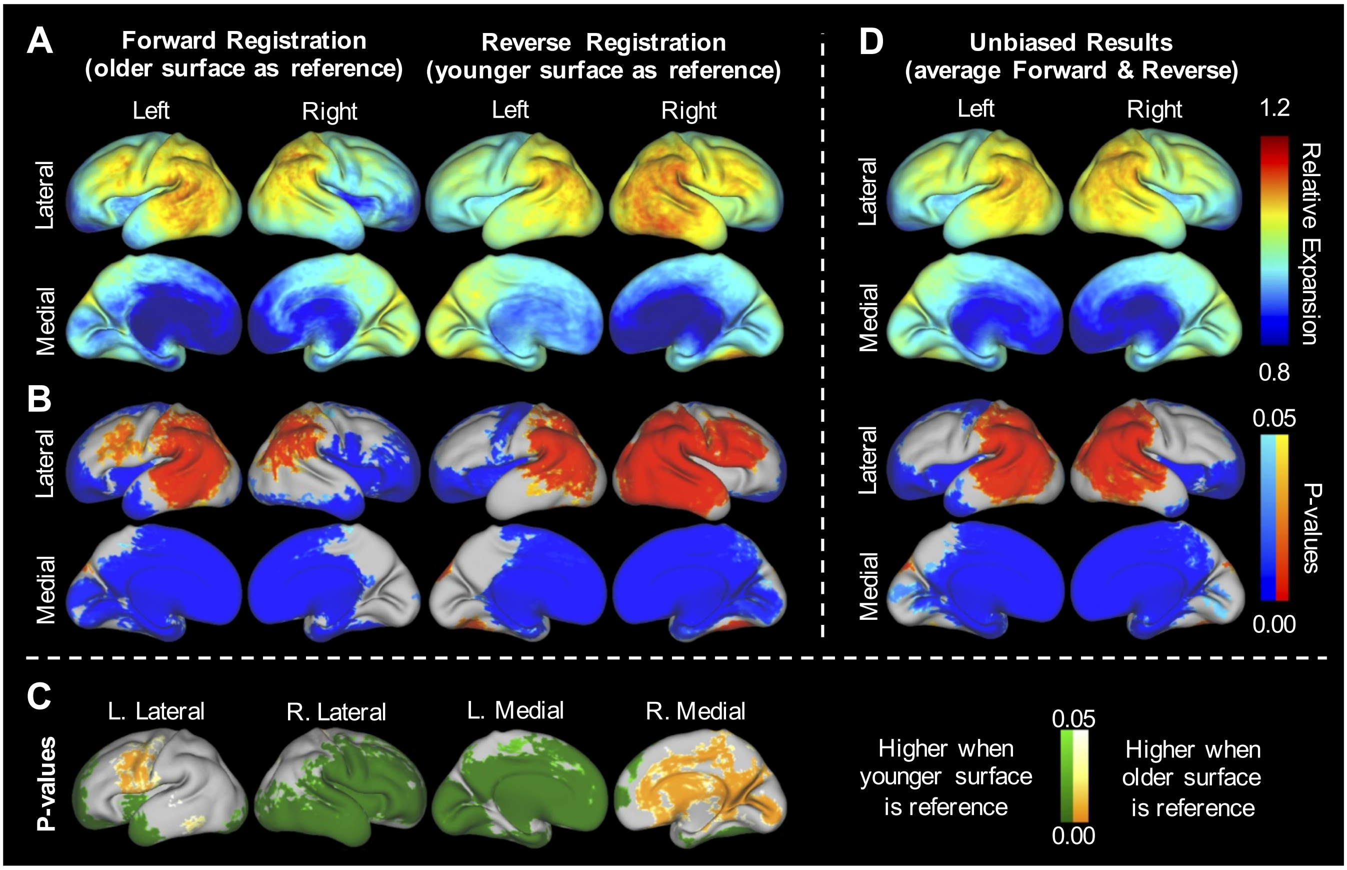

Fig. S3. Averaging forward and reverse registrations to eliminate bias. (*A*) For forward (*Left*) and reverse (*Right*) registration, a map of mean relative expansion is shown for 30 wk PMA to 38 wk PMA (n = 20). (*B*) Areas of statistical significance corresponding to the relative expansion maps shown in *A*, where red is significantly higher than the global average and blue is significantly lower than the global average. Since here we are interested in the effects of registration, which includes registration of the noncortical medial wall, the medial wall was not excluded from this statistical analysis. (*C*) Testing paired differences between forward (*Left*) and reverse (*Right*) registrations reveals significant regional differences. Note similarity between the right lateral and left medial walls, as well as dissimilarity between corresponding right and left regions. (*D*) Averaging forward and reverse registration effectively eliminates this bias, resulting in similar maps for *Right* and *Left*.

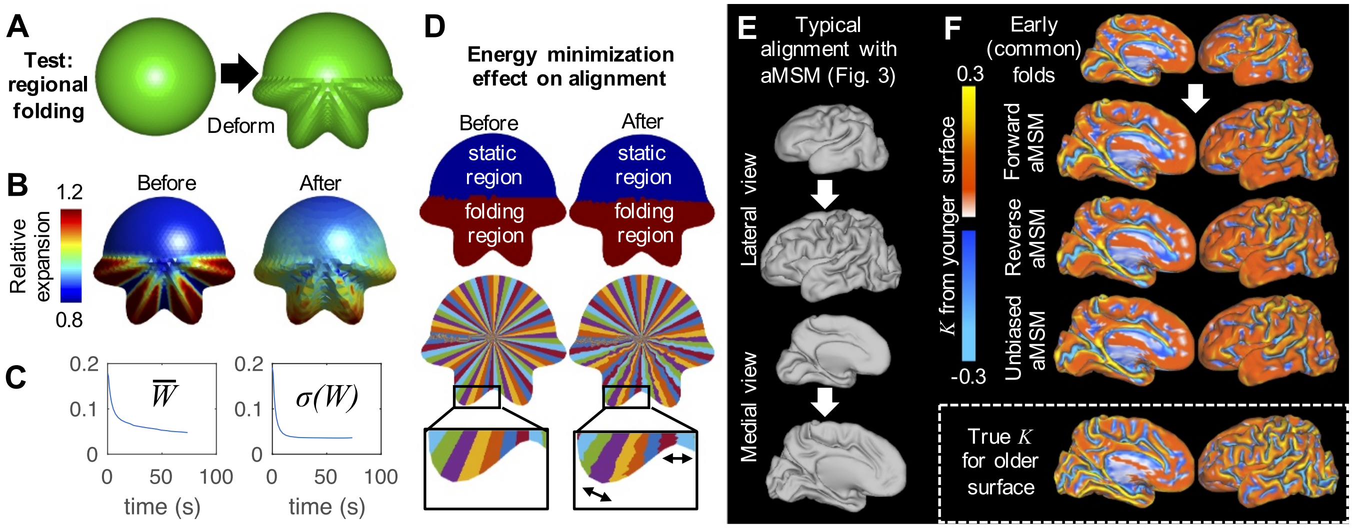

Fig. S4. Strain energy minimization does not adversely affect alignment of folds. (*A*) Effect of strain energy minimization on drift was explored by considering asymmetric (regional) folding of a sphere. (*B* and *C*) Strain energy minimization (using $\kappa = 10\mu$) approximates the converged solution at $t = 70$ s, shown in *B* as the average and SD of strain energy density, $\bar{W}$ and $\sigma(W)$, approach a constant value. (*D*) Two artificial segmentations (based on original angle Φ) are shown for the aligned geometry before and after strain energy minimization to visualize the final locations of points. (*E* and *F*) Effects of aMSM strain energy minimization do not appear to impede qualitative alignment of folds. Regional expansion patterns for this subject are shown in Fig. 3. By plotting K for early folds, we see that reasonable alignment of these early folds is maintained on the corresponding older surface after aMSM including strong regularization (strain energy minimization). (*F*, *Inset*) Older folding pattern is shown for reference.

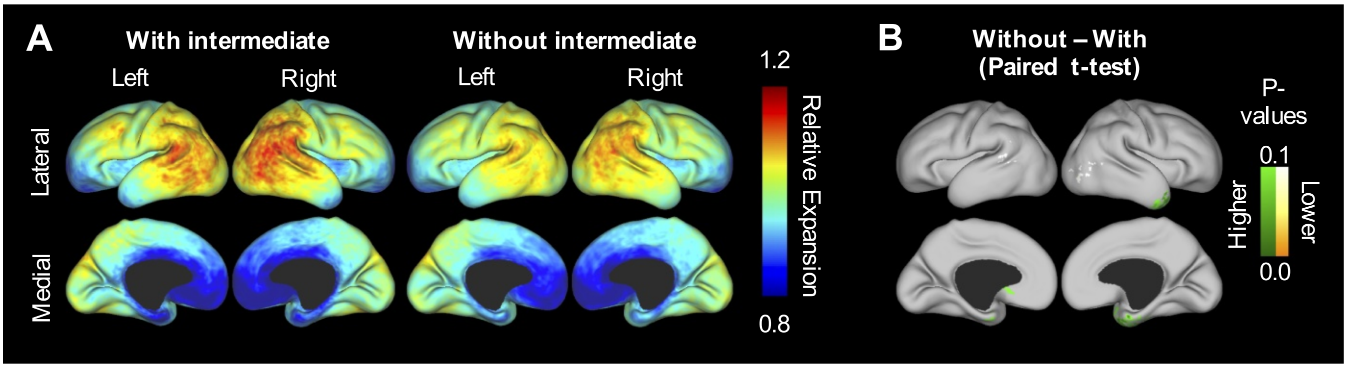

Fig. S5. Effect of time interval between scans. (*A*) For registration with (*Left*) and without (*Right*) an intermediate time point, maps of mean relative expansion are shown for 30 ± 1 wk PMA to 38 ± 2 wk PMA (n = 8, noninjured1–8 in Table S4). (*B*) Testing paired differences with and without the intermediate step reveals only a few small areas of statistical significance. Green denotes areas where relative expansion was higher without an intermediate step, and yellow denotes areas where relative expansion was lower without an intermediate step. Note that to visualize small differences that do exist, and account for low sample size, the threshold for plotting has been raised to $P = 0.1$. Only the dark green region of the right temporal lobe was significant with $P < 0.05$.

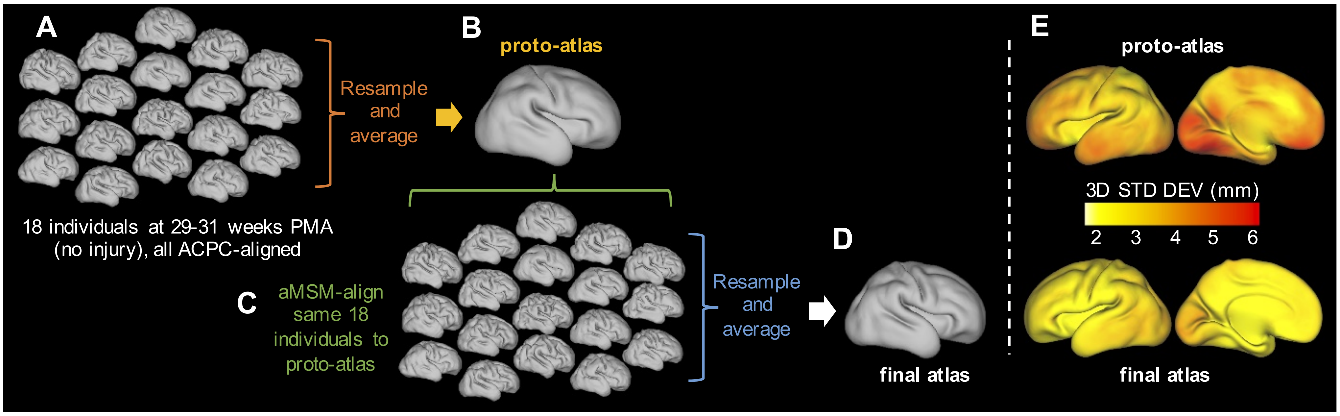

Fig. S6. (*A*–*E*) Atlas generation and aMSM improvement (reduction in 3D dispersion). Individual surfaces (*A*) are resampled and averaged to form a proto-atlas (*B*). Individual surfaces are then registered to the proto-atlas (*C*), and averaged to form the final atlas surface (*D*). (*E*) The final atlas surface exhibits reduced variability with respect to individual surfaces than the proto-atlas.

Table S1. Statistical improvements due to aMSM alignment (n = 10 for each column)

	Wk, PMA			
Parameter	28–30	30–34	34–38	30–38
P before, affine registration only	0.31 ± 0.09	0.32 ± 0.07	0.27 ± 0.13	0.14 ± 0.08
P after, aMSM registration	0.70 ± 0.14	0.81 ± 0.06	0.87 ± 0.03	0.68 ± 0.08
$E/\mu A$ before, affine registration only	1.92 ± 0.45	1.83 ± 0.33	1.87 ± 0.37	3.70 ± 0.65
$E/\mu A$ after, aMSM registration	0.59 ± 0.29	0.61 ± 0.26	0.60 ± 0.33	2.19 ± 0.58

For statistical analysis of aMSM performance, right and left hemisphere results are combined from five subjects scanned at all four time points ($n = 10$ per group). This includes one injured subject (small focal hemorrhagic lesion) that was excluded from analysis of noninjured development in the main results ($n = 4$ in Fig. 5*A*). P represents Pearson's correlation coefficient between curvatures, such that this value approaches 1 with improved alignment. $E = \int W(A)\,\mathrm{d}A$ represents total strain energy across the anatomical surface, here normalized by shear modulus (μ) and total surface area (A). Values are reported as mean ± SD.

Table S2. Linear fits for vertices 1–10 in Fig. 6: growth rate ($\dot{g}$, %/wk) vs. PMA

Vertex	Description	$\dot{g}_{28,L}$	$\dot{g}_{28,R}$	$\ddot{g}_L$	$\ddot{g}_R$	P_L	P_R	p_L	p_R	L/R
1	Prefrontal cortex, lateral	11	12	0.14	0.00	0.15	0.00	0.449	0.995	—
2	Frontal lobe, lateral	13	14	0.20	−0.06	0.16	−0.05	0.436	0.806	—
3	Early somatosensory-motor cortex, lateral	16	17	−0.45	−0.71	−0.43	−0.57	0.026	0.002	*/**
4	Parietal lobe, lateral	13	17	0.31	−0.13	0.27	−0.09	0.174	0.646	—
5	Occipital lobe, lateral	15	16	−0.20	−0.25	−0.18	−0.22	0.377	0.275	—
6	Parietal lobe, lateral	12	15	0.30	−0.12	0.33	−0.18	0.088	0.376	—
7	Insula, lateral	14	18	−0.53	−0.97	−0.50	−0.64	0.007	<0.001	**/**
8	Early somatosensory-motor cortex, medial	16	15	−0.57	−0.62	−0.53	−0.48	0.004	0.011	**/*
9	Early visual cortex, medial	17	19	−0.63	−0.99	−0.41	−0.64	0.033	<0.001	*/**
10	Frontal lobe, medial	11	12	0.08	−0.19	0.10	−0.21	0.629	0.290	—

Labels 1–10 correspond to locations denoted in Fig. 6 for left (L) and right (R) hemispheres. Values are shown for 28-wk intercept ($\dot{g}_{28}$), slope ($\ddot{g}$), Pearson's correlation coefficient, and P-value. Trend significance for L/R hemispheres is denoted in rightmost column with $^*P < 0.05$, $^{**}P < 0.01$.

Table S3. Demographic information for studied cohort ($n = 30$)

Variable	No significant injury, $n = 24$	Injured, $n = 6$
Gestational age at birth, wk	27 ± 1	26 ± 2
Birth weight, g	976 ± 226	898 ± 239
Head circumference at birth, cm	25 ± 2	24 ± 2
Male	50% (12)	50% (3)
Caucasian	46% (11)	67% (4)
CRIB score at birth	10 ± 2	12 ± 3
Time on ventilator, h	24 (0–792)	1104 (24–1,176)
Sepsis	16% (4)	50% (3)
Intrauterine growth restriction	13% (3)	0% (0)
Head circumference at final scan, cm	33 ± 2	33 ± 2
PMA at final scan, wk	37 ± 1	37 ± 1

The above statistics are formatted to denote one of the following: mean ± SD% (n) or median (min–max). Subjects were excluded from group analysis due to (*i*) small grade IV IVH and focal cerebellar hemorrhage on left hemisphere (used in Table S1), (*ii*) grade IV IVH on right hemisphere, (*iii*) grade II IVH and below average cortical surface area/delayed folding, (*iv*) bilateral grade IV IVH (used in Fig. 6*B*), (*v*) bilateral grade IV IVH, or (*vi*) left ventricular dilation. CRIB, Clinical Risk Index for Babies.

Table S4. PMAs and time steps for individuals ($n = 30$)

Subject	PMA1	PMA2	PMA3	PMA4	PMA2–PMA1	PMA3–PMA2	PMA4–PMA3	PMA4–PMA2
Noninjured1	28	30	33	38	2.3	2.7	5.3	8.0
Noninjured2	27	31	33	37	4.1	2.0	3.9	5.9
Noninjured3	27	29	33	36	2.0	3.1	3.6	6.7
Noninjured4′	27	30	34	36	2.9	4.1	2.1	6.3
Noninjured5		29	32	37		3.0	5.0	8.0
Noninjured6		31	33	37		2.0	4.1	6.1
Noninjured7		30	34	38		4.1	3.7	7.9
Noninjured8		29	33	36		4.1	2.9	7.0
Noninjured9			33	37			4.7	
Noninjured10			36	39			3.3	
Noninjured11			35	40			4.6	
Noninjured12			33	36			3.0	
Noninjured13		32		39				7.0
Noninjured14		29		38				8.9
Noninjured15		30		38				8.4
Noninjured16′		30		40				10.1
Noninjured17		30		37				7.7
Noninjured18		29		36				7.6
Noninjured19		30		36				5.6
Noninjured20		31		38				7.0
Noninjured21′		29		37				8.3
Noninjured22		30		35.9				5.1
Noninjured23		30		40				10.0
Noninjured24		32		37				4.9
Injured1	27	31	34	37	3.3	3.4	3.4	6.9
Injured2		31	34	38		3.4	3.6	7.0
Injured3			33	38		4.9	4.3	9.1
Injured4			35	37			2.0	
Injured5			34	37			3.0	
Injured6		31		36				5.7

′denotes noncystic white matter injury in noninjured subject.